On the Discretization of the Integral Equation Describing Scattering by Rough Conducting Surfaces

Jakov V. Toporkov, *Student Member, IEEE,* Roger T. Marchand, *Member, IEEE,* and Gary S. Brown, *Fellow, IEEE*

***Abstract*— Numerical simulations of scattering from one-dimensional (1-D) randomly rough surfaces with Pierson–Moskowitz (P–M) spectra show that if the kernel (or propagator) matrix with zeros on its diagonal is used in the discretized magnetic field integral equation (MFIE), the results exhibit an excessive sensitivity to the current sampling interval, especially for backscattering at low-grazing angles (LGA's). Though the numerical results reported in this paper were obtained using the method of ordered multiple interactions (MOMI), a similar sampling interval sensitivity has been observed when a standard method of moments (MoM) technique is used to solve the MFIE. A subsequent analysis shows that the root of the problem lies in the correct discretization of the MFIE kernel. We found that the inclusion of terms proportional to the surface curvature (regarded by some authors as an additional correction) in the diagonal of the kernel matrix virtually eliminates this sampling sensitivity effect. By reviewing the discretization procedure for MFIE we show that these curvature terms indeed must be included in the diagonal in order for the propagator matrix to be represented properly. The recommended current sampling interval for scattering calculations with P–M surfaces is also given.**

***Index Terms*— Electromagnetic scattering, numerical analysis, Pierson–Moskowitz spectrum, rough surfaces.**

I. Introduction

NUMERICAL solution techniques play an increasingly important role in understanding and predicting scattering from randomly rough surfaces. Recently, a new and powerful iterative numerical technique, called the method of ordered multiple interactions (MOMI), has been proposed by Kapp and Brown for solving the magnetic field integral equation (MFIE), which describes the current induced on a perfectly conducting surface [1]. A similar technique called "forward–backward" has been proposed by Holliday *et al*. [2]. For rough surfaces, MOMI has no apparent convergence problems with very few iterations being completely adequate to describe the scattered field. This rapid convergence makes MOMI very effective computationally and the technique makes extensive numerical simulations of scattering from quite large surfaces possible. This attribute is particularly important for low-grazing angles (LGA's) of incidence.

Manuscript received April 17, 1997; revised September 23, 1997. This work was supported in part by the U.S. Army Research Office, the Office of Naval Research, and the Office of the Assistant Secretary of Defense for C3I by a subcontract through the Lawrence Livermore National Laboratory, Livermore, CA.

The authors are with the Physics Department and the Bradley Department of Electrical Engineering, Virginia Polytech Institute, Blacksburg, VA 24061 USA.

Publisher Item Identifier S 0018-926X(98)01043-6.

Before any numerical technique can be applied, the integral equation should be discretized, i.e., cast in a vector–matrix form. Clearly, the discretization can affect the accuracy of the computed solutions. When studying scattering from one-dimensional (1-D) random surfaces with ocean-like Pierson–Moskowitz (P–M)-type spectra, we found that questions regarding the stability of the solution with respect to sampling interval need to be addressed and that these questions are tied to the understanding of a role of the so-called "curvature term" in the propagator.

In regard to the MFIE, there has been some discussion [3], [4] on whether the curvature term (a term which is proportional to the surface curvature[1]) should be included in the diagonal of the propagator matrix in the discretized equation and how this term affects both the traditional method of moments (MoM) and MOMI solutions. For P–M surfaces, we observed that using a propagator matrix without the curvature term can result in a significant sensitivity in the calculated field to changes in the sampling interval—an effect that is not present for surfaces with Gaussian spectrum. This effect is pronounced in the case of horizontal polarization for backscattering at LGA's and is not very evident for vertical polarization. It appears to be tied to the small-scale (high-frequency) surface curvature, which is characteristic of the P–M spectrum. A stable result can be eventually achieved by decreasing the sampling interval, which, of course, increases the matrix dimension and computational expense of the algorithm. If, however, the curvature terms are included in the diagonal of the propagator matrix, the stable result is obtained at much larger sampling intervals and no drastic increase in a sampling rate is necessary.

This finding prompted us to take a more in-depth look at how the discretization of MFIE is performed, what the role of the curvature term is, and if it should appear in the propagator matrix as a result of discretization. Shapes of the spectra for the currents and the propagator entering the MFIE for P–M surfaces suggest that they can be treated as band-limited functions, with the upper wavenumber (or spatial frequency) beyond which the spectra are assumed to effectively vanish being related to the cutoff in P–M spectrum. Consequently, the sampling theorem can be applied to discretize the MFIE. This consideration suggests choosing the sampling interval based, in general, on *both* the electromagnetic wavelength and the

[1] We are indebted to one of the reviewers for pointing out the fact that curvature is classically defined as $\zeta_{xx}/(1+\zeta_x^2)^{3/2}$ for 1-D surfaces. However, as used herein, the term "curvature" will refer to the second surface derivative ζ_{xx}.

surface spectral cutoff. Also, it shows that the curvature term, in fact, should appear on the diagonal of the propagator matrix that results from its discretization by sampling and that no higher order corrections should be included in either the off-diagonal or diagonal terms. It should be stressed that although we used MOMI as the core of our numerical algorithm, the discussion of discretization refers to the original MFIE before it is reformulated into MOMI. That is why we fully expect that similar problems with sampling stability, when the curvature terms are left out of the diagonal of the propagator matrix, will be observed no matter what numerical method is used to solve the discretized MFIE.

II. MFIE for Two-Dimensional Scattering Problem and the MOMI

The MFIE for a two-dimensional (2-D) scattering problem with a 1-D rough surface and its solution by MOMI are discussed in [1]. An extensive and very detailed discussion of the subject is given in [3]. Here we intend to give only a brief review of the results that will be used in later sections. All fields and currents are assumed to have a time-harmonic dependence of the form $\exp(j\omega_0 t)$.

The idea behind the MFIE is as follows. An incident field illuminating a perfectly conducting surface excites surface currents, which radiate and give rise to a scattered field. By writing expressions for the total field and bringing the observation point to the surface, one obtains an integral equation for these surface currents (which, in the 2-D case, are readily expressed in terms of the E or H field). Once this integral equation is solved and surface currents are known, the scattered field can be found using an appropriate off-surface propagator.

For the surfaces we are interested in it is convenient to work in Cartesian coordinates with the horizontal x axis chosen in the mean surface plane. The surface height above the mean surface plane is given by a function $z = \zeta(x)$. It is assumed that the surface is a perfect electric conductor (PEC) extending from minus infinity to infinity in x. For such a surface illuminated by an incident field, the MFIE will have the form

$$J(x) = J^i(x) + \int_{\mathrm{X}} P(x,\, x')J(x')\,dx' \tag{1}$$

where $J(x)$ is the surface current to be determined, $P(x,\, x')$ is an integral kernel or propagator, and $J^i(x)$ is a forcing term due to the incident field. The domain over which the integration is performed and where all functions are defined should in principle be infinite, but if some taper for the incident field is assumed, in practice, one can usually choose it to be finite. For vertical polarization (H^i tangential to the surface) the quantities involved in (1) are

$$J^i(x) = 2H^i(x,\, z)|_{z=\zeta(x)} \tag{2a}$$

$$P(x,\, x') \equiv 2\,\frac{\partial G(x,\, x')}{\partial n'}\sqrt{1+\zeta_x^2(x')}. \tag{2b}$$

For horizontal polarization (E^i tangential to the surface) we have the following:

$$J^i(x) = 2\,\frac{\partial E^i(x,\, z)}{\partial n}\bigg|_{z=\zeta(x)} \tag{3a}$$

$$P(x,\, x') \equiv -2\,\frac{\partial G(x,\, x')}{\partial n}\sqrt{1+\zeta_x^2(x')}. \tag{3b}$$

In (2) and (3), $H^i(x,\, z)$ and $E^i(x,\, z)$ represent incident magnetic or electric fields, respectively, $G(x,\, x')$ is the free-space Green's function and $\partial/\partial n$ is a derivative along the surface normal at a given point. The factor $\sqrt{1+\zeta_x^2(x')}$ included in the propagator results from converting an integration along the surface to integration along the mean surface plane. In the case of vertical polarization the current $J(x)$ is actually the total magnetic field on the surface, while in the case of horizontal polarization $J(x)$ is the normal derivative of the total electric field on the surface. The forcing term $J^i(x)$ is often referred to as a "Kirchhoff current."

The normal derivatives of the Green's function are

$$\frac{\partial G(x,\, x')}{\partial n'} = \frac{k_0}{4j}\,\frac{-\zeta_{x'}(x')(x-x')+\zeta(x)-\zeta(x')}{\sqrt{1+\zeta_{x'}^2(x')}\,\sqrt{(x-x')^2+[\zeta(x)-\zeta(x')]^2}} \times H_1^{(2)}\Big\{k_0\sqrt{(x-x')^2+[\zeta(x)-\zeta(x')]^2}\Big\} \tag{4}$$

$$\frac{\partial G(x,\, x')}{\partial n} = -\frac{k_0}{4j}\,\frac{-\zeta_x(x)(x-x')+\zeta(x)-\zeta(x')}{\sqrt{1+\zeta_x^2(x)}\,\sqrt{(x-x')^2+[\zeta(x)-\zeta(x')]^2}} \times H_1^{(2)}\Big\{k_0\sqrt{(x-x')^2+[\zeta(x)-\zeta(x')]^2}\Big\} \tag{5}$$

where $H_1^{(2)}$ is a first-order Hankel function of the second kind and k_0 is the free-space electromagnetic wavenumber. It should be pointed out that although the derivation of (1) involves removal of singularity and therefore the principal value of the integral should be taken, it turns out that in the 2-D case, integrals of the type appearing in (1) with kernels given by (2b) or (3b) always converge and taking a Cauchy principal value is not necessary [5].

Once (1) is solved, the scattered field in a far zone at a distance r from the center of the illuminated part of the surface can be found as

$$F^s = \frac{e^{-j\pi/4}}{2\sqrt{2\pi k_0}}\,\frac{e^{-jk_0 r}}{\sqrt{r}}\int_{\mathrm{X}} Q(x,\theta_s)J(x)\,dx. \tag{6}$$

For vertical polarization we solve for magnetic field, $F^s = H^s$ and the integral kernel is

$$Q(x,\,\theta_s) = jk_0[-\zeta_x(x)\sin\,\theta_s + \cos\,\theta_s]\exp\{jk_0[x\sin\,\theta_s + \zeta(x)\cos\,\theta_s]\}. \tag{7}$$

In the case of horizontal polarization one can solve for electric field, i.e., $F^s = E^s$ and

$$Q(x,\,\theta_s) = -\exp\{jk_0[x\,\sin\,\theta_s + \zeta(x)\cos\,\theta_s]\}\sqrt{1+\zeta_x^2(x)}. \tag{8}$$

The scattering angle θ_s appearing in (6)–(8) is defined with respect to the vertical (z) axis and is assumed to be positive in a clockwise direction. Equation (6) with (7) and (8) can be

obtained by using the far-field expansion of either the Green's function (horizontal polarization) or its normal derivative (vertical polarization).

In the case of arbitrarily rough surface, no exact analytical solution of the MFIE (1) is available, but for each given surface and an incident field, it can be solved numerically. To do this, the (1) should be discretized, i.e., put in the vector–matrix form

$$J = J^i + PJ. \tag{9}$$

In (9), J and J^i are vectors and P is a square propagator matrix. For rough surfaces it is common, e.g., [1], [6], to discretize the MFIE by taking values of the surface height, current, and propagator at discrete points $\{x_m\}$, which form a uniform grid with some spacing Δx. That is, the mth element of the surface current vector, the mth element of the Kirchhoff current vector and the (m, n)th element of the propagator matrix are, respectively

$$J_m = J(x_m), \quad J_m^i = J^i(x_m)$$

and

$$P_{mn} = P(x_m, x_n)\Delta x. \tag{10}$$

The diagonal terms ($m = n$) of the propagator matrix may require separate treatment, as will be described below. Following the discretization, a number of numerical techniques can be applied; the traditional MoM solution to (9) would be

$$J = (I - P)^{-1} J^i \tag{11}$$

although it is usually more practical to solve a set of linear equations in the form $(I-P)J = J^i$. In MOMI, the propagator matrix P is split in the lower and upper triangular matrices L and U; $P = L + U$. It is shown in [1] that (9) can be then cast in the following form:

$$J = (I-U)^{-1}(I-L)^{-1}J^i + (I-U)^{-1}(I-L)^{-1}LUJ \tag{12}$$

I being an identity matrix. This equation can now be iterated with the so-called "new Born term"

$$J_B \equiv (I - U)^{-1}(I - L)^{-1} J^i \tag{13}$$

serving as the zeroth-order iterate. The solution is then expressed in terms of a series (some operator identities and rearrangements have to be used, cf. [1]):

$$J = (I - U)^{-1} \sum_{p=0}^{\infty} \{[(I - L)^{-1} - I][(I - U)^{-1} - I]\}^P \cdot (I - L)^{-1} J^i \tag{14}$$

which is the form used in our numerical algorithm. Note that due to the triangular nature of matrices $(I - U)$ and $(I - L)$ no actual matrix inversion is necessary, forward or back substitution can be used and this eliminates the necessity to store and invert the propagator matrix. In fact, it turns out that very few terms in the sum in (14) are needed to achieve sufficient accuracy. For the rough surfaces we worked with, we found that the new Born term (13) often gives a reasonable answer and that two iterations above the new Born term are more than adequate.

The discretization of the MFIE can affect the accuracy of its solution and the calculated scattered field. One parameter that can obviously have an impact and whose choice should be addressed is the sampling interval Δx. Also, there have been different treatments of the diagonal elements of the propagator matrix in (10). In the original version of MOMI [1] the diagonal elements of the propagator matrix P_{mm} were set to be zero. Other authors [6] include in the diagonal a term that is proportional to the second derivative of the surface height and is often referred to as a "curvature term":

$$P_{mm} = \pm \frac{\zeta_{xx}(x_m)}{2\pi[1 + \zeta_x^2(x_m)]} \Delta x. \tag{15}$$

In (15), the upper sign corresponds to the case of vertical polarization and the lower to the horizontal polarization. In [1], it is argued that this term can be neglected if it is small compared to one, which can always be achieved by choosing Δx sufficiently small. The question about the inclusion of this term was also addressed in [3] and [4]. One of the conclusions was that the curvature term does not affect the rate of MOMI convergence. It was also reported that for one sample sinusoidal surface with high curvature and the incident field coming at 45° with respect to the normal, the inclusion of the curvature term did permit an increase in the sampling interval resulting in the same scattered field as would be obtained without the curvature term but with tighter sampling. Nevertheless, for a randomly rough surface with Gaussian spectrum and root mean square (rms) slopes as high as 45° illuminated at the incident angle of 85°, no effects related to inclusion or exclusion of the curvature term were observed. The study in [3] regarded the curvature term as an additional correction to the already extracted self term and pointed out that it may be inconsistent to include this correction on the diagonal of the propagator matrix and not include similar corrections proportional to higher surface derivatives in off-diagonal terms.

In the next section, we present the results of numerical calculations of scattering from randomly rough surfaces with P–M spectra and these results suggest that for such surfaces the curvature term can play an important role and should be included in the diagonal of the propagator matrix. In Section IV we will discuss the procedure that leads to the discretized MFIE (9), (10), and suggest a choice of the sampling interval for P–M surfaces. It will be shown that *once the proper sampling interval is chosen, the curvature term in* (15) *must appear on the diagonal of the propagator matrix, the off-diagonal terms should be samples of the propagator as given by* (10), *and there should be no higher order corrections to either the diagonal or the off-diagonal terms.*

III. Simulation Results for Scattering from 1-D Pierson–Moskowitz Surfaces

We used MOMI to calculate the scattering from ocean-like randomly rough perfectly conducting surfaces described by a P–M spectrum. For the 1-D surfaces we used a 1-D version

of the P–M spectrum proposed by Thorsos [7]

$$W(K) = \frac{\alpha}{4|K|^3} \exp\left\{-\frac{\beta g^2}{K^2 U^4}\right\}. \tag{16}$$

In (16), K is the spatial wavenumber (which can be both positive and negative), U is the windspeed at a height of 19.5 m, $g = 9.81$ m/s^2 is gravity acceleration and other constants are $\alpha = 8.10 \times 10^{-3}$ and $\beta = 0.74$. The mean-square surface height is

$$h^2 = \int_{-\infty}^{\infty} W(K)\, dK = \frac{\alpha U^4}{4\beta g^2}. \tag{17}$$

The spectrum (16) has a peak at a wavenumber

$$K_p = \sqrt{\frac{2\beta}{3}}\, \frac{g}{U^2} \tag{18}$$

which can be interpreted as corresponding to the dominant wave having the wavelength

$$\Lambda_p = \frac{2\pi}{K_p} = \pi \sqrt{\frac{6}{\beta}}\, \frac{U^2}{g}. \tag{19}$$

The P–M spectrum (16) has only one variable parameter, the windspeed U, which controls both the mean-square surface height and the dominant surface wavelength (and also the surface correlation length which can be shown to be closely related to Λ_p), as can be seen from (17) and (19).

A characteristic feature of the P–M spectrum (16) is its power-law behavior at large surface wavenumbers K. In fact, due to this behavior integrals of the type (17) describing the mean-square slope, mean-square curvature, and all higher derivatives will be divergent unless some cutoff wavenumber K_c is chosen, i.e., the spectrum assumes the form

$$W_1(K) = \begin{cases} W(K), & |K| < K_c \\ 0, & \text{otherwise} \end{cases}. \tag{20}$$

This means that for Pierson–Moskowitz surfaces the short-wave surface structure is the major contributor to the mean-square surface slope and higher derivatives. A particular choice of K_c is likely to affect scattering from the surface, especially at LGA's, and this subject probably deserves a separate study. In natural ocean surfaces such a cutoff occurs due to viscous damping mechanisms and can vary if, for example, pollutants or surfactants are present. In most of our simulations we fixed the cutoff to be five times the electromagnetic wavenumber, i.e.,

$$K_c = 5k_0 \tag{21}$$

which definitely includes all potential Bragg scatterers.

The electromagnetic wavelength we use is $\lambda_0 = 23$ cm. We chose to work with surfaces corresponding to the windspeed $U = 5$ m/s. This yields the dominant surface wavelength, as determined from (19), to be $\Lambda_p = 22.8$ m $= 99.1\lambda_0$. This allowed us to work with surface sizes that included several dominant wavelengths but still were not very large electrically. It should be pointed out that as one moves toward grazing, other considerations come into play and require increasingly larger surfaces to be used in the simulations. The rms surface height corresponding to this windspeed is [from (17)] $h = 0.133$ m $= 0.58\lambda_0$.

The incident field is taken to be a plane wave with a modified Gaussian taper suggested by Thorsos [6]

$$F^i(x, z) = \exp\{-jk_0(x \sin\theta_i - z\cos\theta_i)[1 + w(x, z)]\} \cdot \exp\left\{-\frac{(x + z\tan\theta_i)^2}{g^2}\right\} \tag{22}$$

where, again, F is either the E or H field, depending on the polarization considered. In (22) the incident angle θ_i is defined with respect to the vertical (z) axis and is assumed to be positive in a counterclockwise direction; g is the parameter that controls the tapering [not to be confused with gravity acceleration in (16)], and $w(x, z) = \{2(x + z\tan\theta_i)^2/g^2 - 1\}/(k_0 g\cos\theta_i)^2$. The choice of $g = L_s/6$ (L_s = finite surface length) gives an acceptable tapering at the edges. In the case of horizontal polarization a normal derivative of (22) is needed to calculate the Kirchhoff current J^i; analytical expression for such a derivative can be easily obtained from (22).

To describe scattering from each surface realization a bistatic normalized radar cross section (NRCS), $\sigma^0(\theta_i, \theta_s)$ can be introduced

$$\sigma^0(\theta_i, \theta_s) = \lim_{r\to\infty} \frac{2\pi r|F^s|^2}{\int |F^i(x, 0)|^2\, dx} \tag{23}$$

where F^s is given by (6). The backscattered NRCS is $\sigma^0_{bsc}(\theta_i) \equiv \sigma^0(\theta_i, -\theta_i)$. $\sigma^0(\theta_i, \theta_s)$ can be averaged over an ensemble of several surface realizations to obtain an average NRCS $\langle\sigma^0\rangle$.

Surface realizations were generated using the spectral technique similar to that described in [6]. First, independent complex Gaussian variables with zero means and variances $W_1(K_l)\Delta K$ are generated at discrete wavenumbers $\{K_l\}$(ΔK is the spacing between adjacent samples in the spectral domain) to represent a spectrum $Z(K_l)$ of a particular surface realization. This is done only for nonnegative wavenumbers since $Z(K_l)$ must possess certain symmetry properties to assure that surface heights are real. Spectra of first and second surface derivatives can be obtained by multiplying $Z(K_l)$ by jK_l and $(jK_l)^2$, respectively. Then, the fast Fourier transform (FFT) is used to calculate the surface heights and values of surface derivatives at discrete values of x. To generate a surface of length L_s, the step size in the spectral domain should be

$$\Delta K = 2\pi/L_s. \tag{24}$$

Inclusion of spectral values within the wavenumber range $\pm K_{\rm up}$ will require the following number of points in the spectral domain:

$$N = \frac{2K_{\rm up}}{\Delta K} = \frac{2K_{\rm up}L_s}{2\pi} = \frac{K_{\rm up}L_s}{\pi}. \tag{25}$$

The same number of points after the FFT represents surface samples over the surface length L_s, which gives a sampling interval on the surface equal to

$$\Delta x = L_s/N = \pi/K_{\rm up}. \tag{26}$$

$K_{\rm up}$ should obviously be chosen at least as large as the spectral cutoff K_c in the P–M spectrum (20). Making it higher does not alter the spectral content of the surface since outside $\pm K_c$ the spectrum $W_1(K)$ is zero anyway, but it results in a smaller sampling interval Δx, as is clear from (26). The largest possible sampling interval needed to represent a surface with spectral cutoff K_c will be $\Delta x_0 = \pi/K_c$, i.e., at least two points per the shortest wavelength present on the surface. For our choice of K_c in (21), this means

$$\Delta x_0 = \pi/(5k_0) = \lambda_0/10. \tag{27}$$

Since a radix 2 FFT is used to compute the surface points from its spectrum, the number of points N must be a power of two. We chose Δx_0 to be our basic sampling interval. Together with $N_0 = 8192 = 2^{13}$ points this provided a surface length $L_s = 819.2\lambda_0$. This surface length was deemed to be acceptable for our study for various reasons but primarily because it contained several dominant surface wavelengths Λ_p. The P–M spectrum in (16) has a peak at K_p that moves closer to zero and becomes sharper as the windspeed U increases. One would like to choose ΔK small enough to represent this peak adequately and certainly not to miss it altogether. This means choosing $\Delta K \ll K_p$ or, equivalently, $L_s \gg \Lambda_p$. The tapering parameter in this case is $g = L_s/6 = 136.5\lambda_0$ which is sufficiently large to use the tapered incident field in (22) safely for incident angles up to 83°–84°. When a smaller sampling interval was needed, we increased $K_{\rm up}$ [cf. (26)]. That is, we kept the random spectral values $Z(K_l)$ already generated the same, added zeros up to the new higher value of $K_{\rm up}$, and then took the FFT of this newly constructed spectrum. This resulted in the generation of the same (but tighter sampled) surface realization. Again, due to the radix 2 FFT used it was convenient to decrease Δx by a factor of two.

The result of the outlined procedure are values of the surface height $\{\zeta(x_m)\}$, slope $\{\zeta_x(x_m)\}$, and second derivative $\{\zeta_{xx}(x_m)\}$ at discrete values of x, $x_m = (m - 1 - N/2)\Delta x$, $m = 1, 2, \cdots, N$. By substituting these values in (2) and (3) [and using (4), (5), and (22)] we get discretized values of the current and propagator shown in (10). To calculate a scattered field from (6), we also take the values of a kernel Q only at points $\{x_m\}$ so the integral in (6) is also replaced by a discrete sum.

We started by applying MOMI with its propagator matrix containing zeros on its diagonal. Fig. 1 shows the calculated bistatic cross section for one surface realization and a horizontally polarized field incident at 80° (only negative scattering angles corresponding to backward scattering are shown). One curve on the graph corresponds to the sampling interval Δx_0 and another to the interval eight times smaller: $\Delta x = \Delta x_0/8$ [the spectral cutoff wavenumber, as has been stipulated, remains the same, as given by (21)]. It can be observed that two curves start showing some differences even at moderate scattered angles and as the observation direction moves toward grazing these differences become more and more pronounced. Similar behavior is observed for bistatic cross sections corresponding to smaller incident angles, although the differences in decibels are, in general, smaller for those angles.

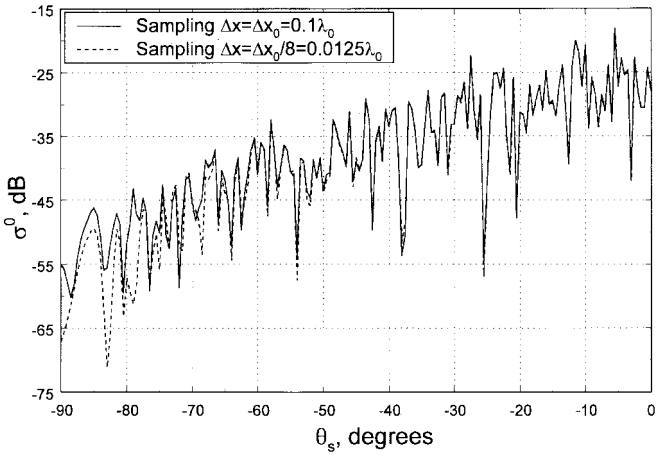

Fig. 1. Bistatic normalized radar cross section (for a single realization of a P–M surface). Horizontal polarization, $\theta_i = 80°$, two MOMI iterations, curvature term not included.

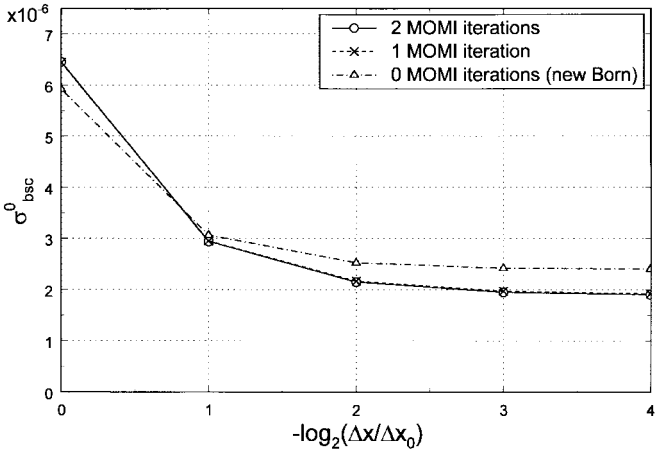

Fig. 2. Normalized radar cross section in the backscattered direction ($\theta_i = 80°$, single realization of a P–M surface) versus sampling interval. Horizontal polarization, curvature term not included.

We observed similar differences in the NRCS when applying MoM (11) with zeros on the diagonal of the propagator matrix, though we had to work with smaller surfaces due to the large memory requirements of MoM.

A typical behavior of the backscattered field as the sampling interval changes is shown in Figs. 2 and 3 ($\theta_i = 80°$). Fig. 2 shows the NRCS, which is proportional to the square of field magnitude and Fig. 3 shows the phase of the scattered field with the factor e^{-jk_0r} that is present in (6) ignored. Each figure displays results calculated using zero, one, and two iterations of MOMI above the new Born term. One can see that points corresponding to one and two iterations of MOMI practically coincide, so MOMI *does converge no matter what sampling interval is chosen, but for different sampling intervals it converges to different values.* Fig. 3 suggests that even for the sampling interval of $\Delta x = \Delta x_0/16 = \lambda_0/160$ the phase of the scattered field still has not reached its final value and would change if we reduced the sampling interval further.

This dependence of the calculated NRCS on the sampling interval appears to be tied to the short wave structure on the surface. Fig. 4 presents bistatic cross sections for hor-

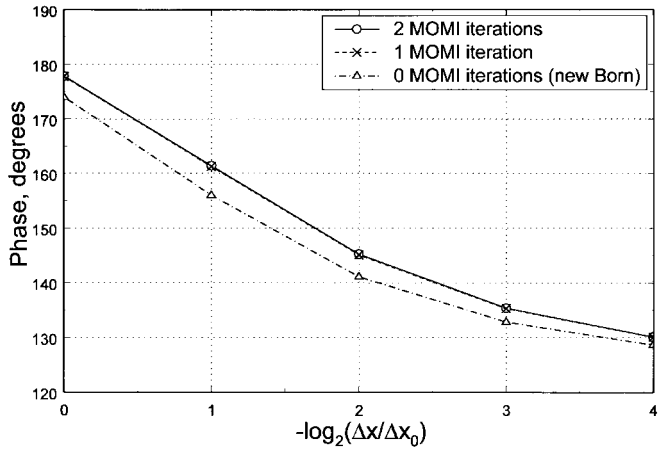

Fig. 3. Phase of the backscattered field ($\theta_i = 80°$, single realization of a P–M surface) versus sampling interval. Horizontal polarization, curvature term not included.

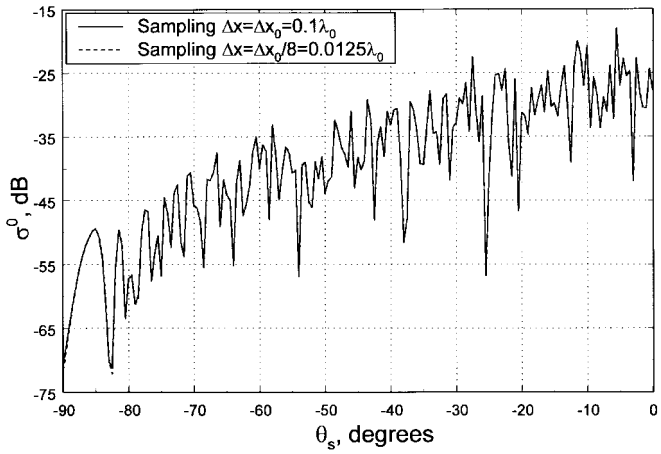

Fig. 5. Bistatic normalized radar cross section (for a single realization of a P–M surface). Horizontal polarization, $\theta_i = 80°$, 2 MOMI iterations, curvature term included.

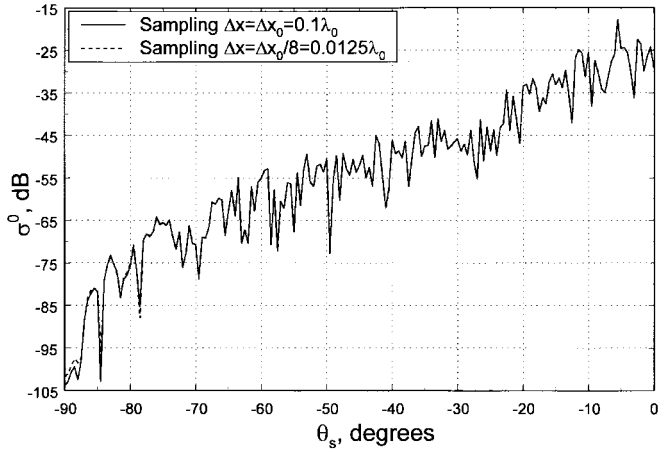

Fig. 4. Bistatic normalized radar cross section (for a single realization of a P–M surface with spectral cutoff wavenumber reduced to $k_0 = 2\pi/\lambda_0$). Horizontal polarization, $\theta_i = 80°$, two MOMI iterations, curvature term not included.

izontal polarization calculated with sampling intervals Δx_0 and $\Delta x_0/8$ for a surface with a spectral cutoff wavenumber $K_{c1} = k_0$ which is five times smaller than the cutoff K_c used in previous simulations. This figure should be compared to Fig. 1 and now one can see almost no differences except for a few nulls near grazing where some discrepancy is not surprising given the extremely low levels. This apparent cause and effect relation between the observed changes in calculated NRCS with the sampling interval and the short-wave components suggests that the effect should not be seen if a surface with Gaussian spectrum is used because it effectively contains no short-wave components since they are exponentially suppressed.

As has been mentioned, it is the short-wave components that are the main contributors to the rms slope and especially the rms curvature of the P–M surface. Consequently, including the curvature terms (15) in the diagonal of the propagator matrix may be one possible remedy to the problem. NRCS calculations with the curvature term included are shown in Fig. 5. The surface is the same as was used for calculations in Figs. 1–3; its spectral cutoff is given by (21). These new results show that the bistatic NRCS calculated with the sampling interval Δx_0 is virtually the same as the NRCS obtained from calculations with a much smaller interval of $\Delta x_0/8$. This presents quite a different picture from the situation shown in Fig. 1. The behavior of the scattered field versus the sampling interval is again examined in Figs. 6 and 7 for backscattering at 80°. Fig. 6 shows that once the curvature term is included, there is no noticeable change in NRCS. In Fig. 7 a slight change in the phase of the calculated backscattered field can be noticed as one moves from the sampling interval of Δx_0 to $\Delta x_0/2$, but after that its value remains constant. As the sampling interval is decreased both the NRCS and phase of the scattered field calculated without curvature eventually converge to their counterparts calculated with the curvature term. Note that the phase of the field calculated without curvature term does not reach this stable value even at a sampling interval as small as $\Delta x_0/16$. *This demonstrates that, with the inclusion of the curvature term, one indeed achieves stability with respect to the sampling interval and obtains the correct values of the scattered field without resorting to the heavy oversampling that would have been necessary otherwise.*

So far we addressed only the case of horizontal polarization. For vertical polarization, we found that when the propagator matrix without the curvature terms is used, the calculated NRCS does not possess the sensitivity to the size of the sampling interval that was observed in the case of horizontal polarization. This fact is demonstrated in Fig. 8, where calculations of the bistatic NRCS for vertical polarization and an incident angle of 80° are presented for two different sampling intervals. Actually, if one examines the absolute difference in a scattered field calculated without the curvature term at two different sampling intervals, this difference will be, on the average, larger for vertical polarization than for horizontal polarization. But since the magnitude of the field scattered in the backward direction is significantly larger in the case of vertical polarization, the relative changes in the field (and, therefore, NRCS) are negligibly small compared to what was observed for the horizontal polarization. Inclusion

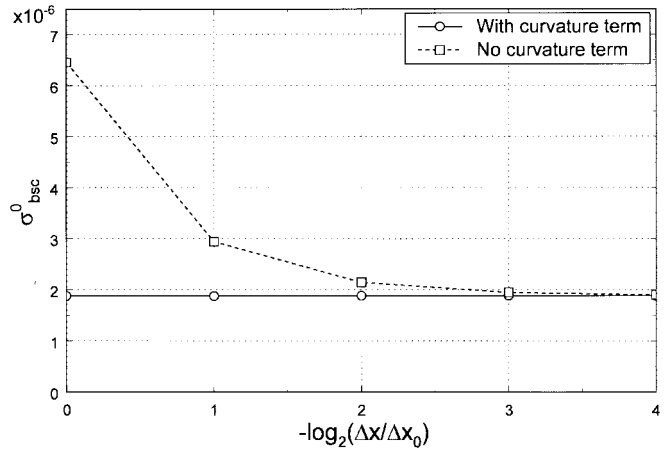

Fig. 6. Normalized radar cross section in the backscattered direction ($\theta_i = 80°$, single realization of a P–M surface) versus sampling interval. Horizontal polarization.

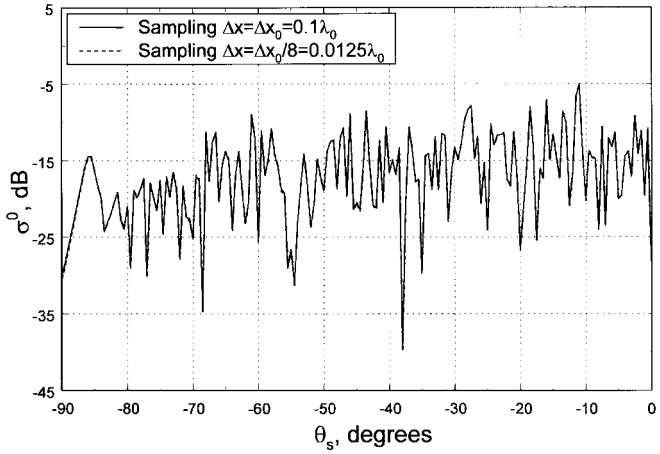

Fig. 8. Bistatic normalized radar cross section (for a single realization of a P–M surface). Vertical polarization, $\theta_i = 80°$, two MOMI iterations, curvature term not included.

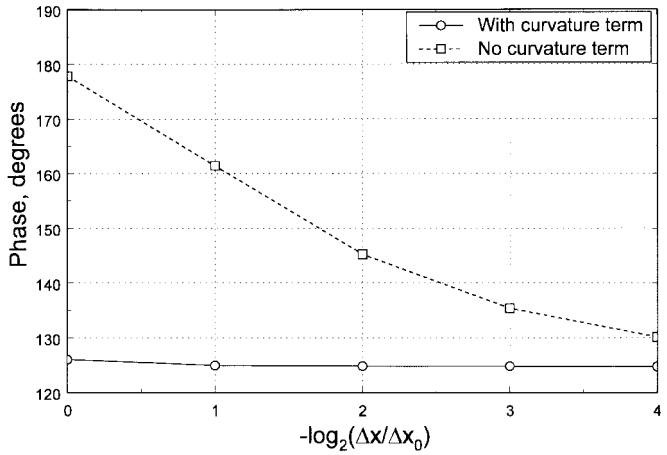

Fig. 7. Phase of the backscattered field ($\theta_i = 80°$, single realization of a P–M surface) versus sampling interval. Horizontal polarization.

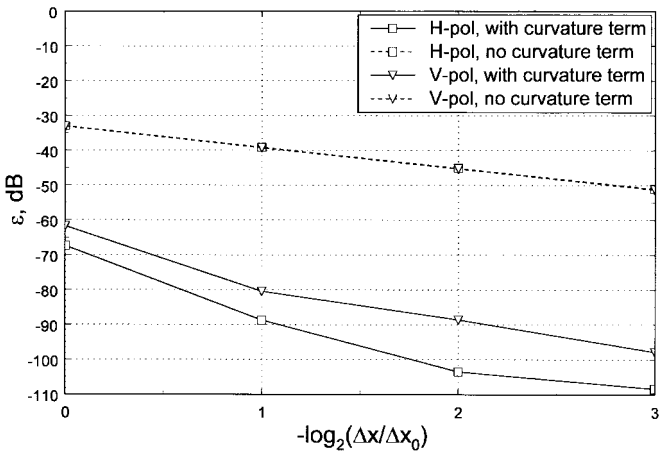

Fig. 9. Relative mean square error in the calculated surface current versus sampling interval. $\theta_i = 80°$, single realization of a P–M surface.

of the curvature terms in the diagonal of the propagator matrix in the case of vertical polarization also significantly reduces variation in the calculated field and the NRCS as one changes the sampling interval but, again, this variation is relatively small from the beginning.

It is interesting to look at the behavior of the relative mean-square error in the current versus sampling. Assuming the current calculated at the smallest sampling interval of $\Delta x_0/16$ with the curvature term included to be the "exact" current J_0, we define the relative mean square error in the current calculated with some sampling interval Δx as

$$\varepsilon(\Delta x) = \frac{1}{||J_0||}\left[\frac{1}{N}\sum_{k=1}^{N}|J_{\Delta x}(x_k) - J_0(x_k)|^2\right]. \quad (28)$$

In (28) the values $\{x_k\}$ are taken with the sampling interval Δx, $J_{\Delta x}$ denotes the current calculated with this sampling interval (with or without the curvature term) and

$$||J_0|| = \frac{1}{M}\sum_{l=1}^{M}|J_0(x_l)|^2 \quad (29)$$

where $M = N_0 \times 16 = 2^{17}$ and $\{x_l\}$ are taken with the sampling interval $\Delta x_0/16$. Only one surface realization is considered. Fig. 9 shows $\varepsilon(\Delta x)$ for the current calculated with and without the curvature term for both horizontal and vertical polarizations and $\theta_i = 80°$. When the curvature term is not included, the relative mean square error in the current is essentially the same for horizontal and vertical polarizations. Yet, as we have seen, in the case of horizontal polarization this error does produce significant relative variations in NRCS, while for vertical polarization, these variations are negligible. This once more confirms the well-known fact that an error in the current does not necessarily translate into a significant error in the scattered field. Each time the sampling interval is divided in half, $\varepsilon(\Delta x)$ for the current without curvature term decreases by approximately 6 dB, which means that rms error in the current decreases by a factor of two. When the curvature term is included, $\varepsilon(\Delta x_0/8)$ is reduced dramatically, with the relative mean square error for horizontal polarization being smaller than that for vertical polarization. Note that $\varepsilon(\Delta x_0)$ for the currents with curvature is well below $\varepsilon(\Delta x_0/8)$ for the currents without curvature.

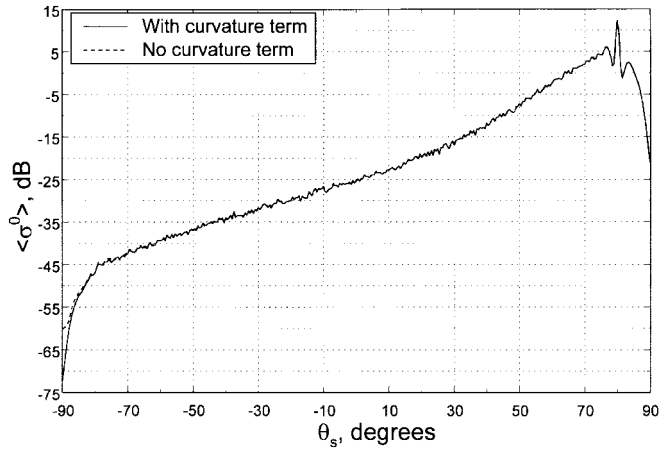

Fig. 10. Average bistatic normalized radar cross section (average over 100 surfaces with P–M spectrum). Horizontal polarization, $\theta_i = 80°$, two MOMI iterations, $\Delta x = \Delta x_0/2 = \lambda_0/20$.

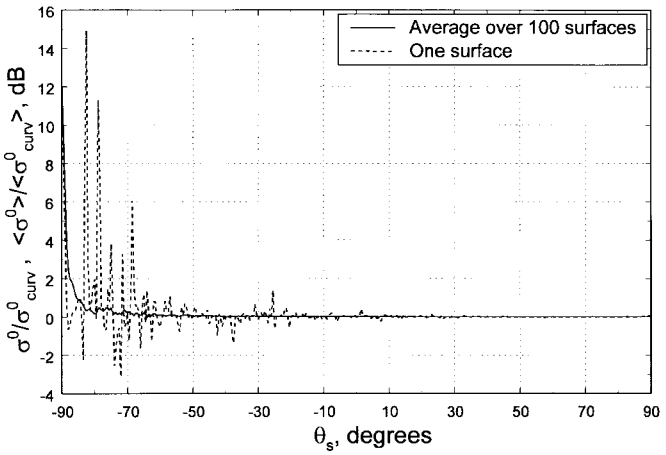

Fig. 11. Ratio (expressed in decibels) of average bistatic normalized radar cross sections calculated without and with the curvature term (average over 100 surfaces with P–M spectrum). Also shown is a similar ratio of normalized radar cross sections corresponding to one P–M surface. Horizontal polarization, $\theta_i = 80°$, two MOMI iterations, $\Delta x = \Delta x_0/2 = \lambda_0/20$.

Finally, let us address the question of how the inclusion or omission of the curvature term affects the average NRCS. Fig. 10 displays the average bistatic NRCS (the average is taken over 100 surfaces) for horizontal polarization and an incident angle of 80° that was calculated with and without curvature term; the mean field was not extracted, so it shows up in the specular direction. The sampling interval of $\Delta x_0/2$ was used. For most of the scattering angles the two curves run on top of each other but as the scattering angle approaches $-90°$, the differences start showing up, with the NRCS calculated without the curvature term having larger values. Around the grazing scattering angle of $-90°$ calculations without the curvature term result in an overestimation of average NRCS by more than 10 dB. Fig. 11 shows the ratio of the average NRCS calculated without the curvature term to the average NRCS with this term. Expressed in decibels, this ratio corresponds to the distance between the curves shown in Fig. 10. For comparison, the similar ratio is plotted in Fig. 11 for only one surface realization. One can see that, in general, the average NRCS shows much less sensitivity to the inclusion or exclusion of the curvature term than the NRCS for a single surface realization. Still, at scattering angles near grazing, even the average NRCS is very sensitive to the presence or absence of the curvature term.

IV. Discretization of the MFIE and the Necessity of the Curvature Term

In the previous section it was shown that when the MFIE is solved for P–M surfaces with the diagonal of the propagator matrix set to zero, in some cases very tight sampling is required to obtain a stable value for the scattered field. However, inclusion of the curvature terms in the diagonal appears to remedy this problem. We now examine the details of discretization to find out why curvature terms should be included in the diagonal of the propagator matrix and whether there should be any higher order corrections, as well as to develop some recommendations for choosing the sampling interval when discretizing the MFIE for P–M surfaces.

The classical MoM approach described in [8] can be applied to discretize the MFIE in (1). Two sets of linearly independent functions $\{e_n(x)\}$ and $\{t_m(x)\}$ (called expansion and testing functions, respectively) and a scalar product $\langle \cdot, \cdot \rangle$ are introduced. The reasonable scalar product of two possibly complex-valued functions f and g can be defined as

$$\langle f(x),\, g(x)\rangle = \int_{\mathrm{X}} f^*(x) g(x)\, dx \tag{30}$$

with the asterisk denoting the complex conjugate. Assuming that the set $\{e_n(x)\}$ is complete for the class of functions that the unknown current $J(x)$ belongs to, one can write

$$J(x) = \sum_n J_n e_n(x) \tag{31}$$

where $\{J_n\}$ are the expansion coefficients. This expression is substituted in (1) and a scalar product is taken of both sides of this equation with each of the testing functions

$$\sum_n J_n \langle t_m(x),\, e_n(x)\rangle = \langle t_m(x),\, J^i(x)\rangle + \sum_n J_n \int_{\mathrm{X}} \langle t_m(x),\, P(x,\, x')\rangle e_n(x')\, dx'. \tag{32}$$

It can be seen that in order for (32) to assume the vector–matrix form (9) with $J = [J_n]$ from (31), an additional multiplication of both sides of (32) by the matrix inverse $[\langle t_m(x),\, e_n(x)\rangle]^{-1}$ is, in general, necessary. However, if we require that

$$\langle t_m(x),\, e_n(x)\rangle = a_m \delta_{mn} \tag{33}$$

(a_m are some positive constants and δ_{mn} is a Kronecker delta), i.e., testing and expansion functions should be mutually orthogonal, the goal is readily achieved with the quantities appearing in (9) being

$$J = [J_n], \quad J^i = \left[\frac{1}{a_m}\langle t_m(x),\, J^i(x)\rangle\right]$$

and

$$P \equiv [P_{mn}] = \left[\frac{1}{a_m}\int_{\mathrm{X}} \langle t_m(x),\ P(x,\ x')\rangle e_n(x')\,dx'\right]. \quad (34)$$

Furthermore, if the expansion functions $\{e_n(x)\}$ are chosen to be orthogonal and $\{t_m(x)\}$ are chosen to belong to the same class of functions, then the completeness of $\{e_n(x)\}$ for this class together with (33) means that $t_n(x) = c_n e_n(x)$ where c_n are nonzero constants, so the expansion and testing functions are essentially the same. If the testing functions are chosen outside the class that $\{e_n(x)\}$ belong to (one can use δ functions as an example), this, of course, is not true.

Our goal is to apply the formalism described above to see how and under what conditions a simple discretization such as (10) is possible. It is tempting to use δ functions as expansion and testing functions because this would immediately formally give the discretized (9) with sampled quantities (10). However, in this case one cannot write an expansion (31) for any reasonable continuous or square-integrable function such as we expect $J(x)$ to be to begin with. Another choice (pursued, for example, in [3]) is to use δ functions as testing functions together with rectangular pulse expansion functions [in this case, for example, (33) can be satisfied]. This approach, however, seems to have its own deficiencies. First, rectangle pulse functions do not form a complete set for the class of continuous functions, so (31) cannot be exact and (9) will involve some error from the start. Further, elements of the discretized propagator will contain integration over the pulse width in x' coordinate

$$P_{mn} = \int_{x_n-\Delta x/2}^{x_n+\Delta x/2} P(x_m,\ x')\,dx' \quad (35)$$

to obtain a simplified form as given by (10) some additional approximations of these integrals will be necessary. In fact, it is the evaluation of these integrals obtained by expanding the propagator in a Taylor series around x_n that led Kapp in [3] to consider the curvature term as an additional correction resulting from accounting for more terms in Taylor series and to argue that these corrections should also be considered for the off-diagonal elements. Still, from this approach, it is not clear what value for the sampling interval (pulse width) should be chosen to discretize the MFIE. It is important to realize that even if the integrals (35) are evaluated *exactly* (or, equivalently, *all* terms in the Taylor expansion of the propagator are accounted for), there will still be some error in the solution due to poor approximation of the continuous current $J(x)$ by rectangular pulses.

In our approach, we will use the sampling theorem and ideas and concepts related to it. Let us first make the following observation: for well-behaved surfaces the limit of (4) and (5) as $x \to x'$ exists; the functions in (4) and (5) can be defined at $x = x'$ to be equal to this limit and, thus, the propagator in (1) is a continuous function. P–M surfaces that we work with have a distinct spectral cutoff, as stated in (20). The hope may be that the current and propagator, being functionally dependent on the surface height, might also have their spectra located predominantly within some finite range of wavenumbers so they can be reasonably regarded as belonging to the class of the functions with finite spectral width. It is known that for the class of band-limited functions that have zero spectral components beyond some wavenumber K_u, the functions

$$s_n(x) = \frac{\sin\,\pi(x/\Delta x - n)}{\pi(x/\Delta x - n)}, \qquad \Delta x = \pi/K_u \quad (36)$$

form a complete set (cf. for example, [9]). These functions are orthogonal with respect to the scalar product (30) (domain X is assumed to be infinite)

$$\langle s_m(x),\ s_n(x)\rangle = \Delta x \delta_{mn}. \quad (37)$$

Any function f of this class of band-limited functions can be expanded in this basis

$$f(x) = \sum_n f_n s_n(x)$$

with expansion coefficients being

$$f_n \equiv \frac{1}{\Delta x}\langle s_n(x),\ f(x)\rangle = f(n\Delta x). \quad (38)$$

The previous two equations are essentially the main result of the sampling theorem indicating that band-limited function can be reconstructed from its properly taken samples using sinc-type basis functions.

The spectra of $J^i(x),\ J(x)$, and $P(x,\ x')$ have a characteristic shape that can be regarded as band-limited and suggests the choice of the wavenumber K_u, beyond which the spectra of all these functions are essentially zero.

Fig. 12 shows a shape of a 2-D Fourier spectrum of the propagator $P(x,\ x')$, as given by (3b) for horizontal polarization and one random surface realization; some coarse-graining was applied to reduce the number of points to plot. Because of computational constraints the spectral cutoff of the surface in this particular case was chosen to be $K_c = 2.5k_0$ Fig. 13 displays the spectrum of the propagator given in (2b) for vertical polarization and the same surface. The spectrum of the propagator consists of two narrow "blades," each having a half-length of K_c, that are centered at $(-k_0,\ k_0)$ and at $(k_0,\ -k_0)$. In the case of horizontal polarization (Fig. 12) these two blades are oriented along the K-axis (which is dual to x-coordinate). So, the spectrum is essentially nonzero only in the rectangular domain with K varying within $\pm(k_0 + k_c)$ and K' varying within the range somewhat larger (by the thickness of the "blades") than $\pm k_0$. Certainly, the spectrum can be considered band-limited within a larger square domain (which is more convenient for our consideration) with the upper limit

$$K_u = k_0 + K_c \quad (39)$$

in both K and K'. The same discussion applies to the vertical polarization propagator (now the picture is turned by 90°) with the same result (39) for the wavenumber domain upper limit K_u.

Fourier spectra of Kirchhoff currents $J^i(x)$ calculated according to (2a) or (3a) and (22) in general have a peak at $K = -k_0 \sin\,\theta_i$ accompanied by a "pedestal" that is centered at the same wavenumber and has the half-width K_c. Examples of such spectra (normalized to their peaks) are shown using a

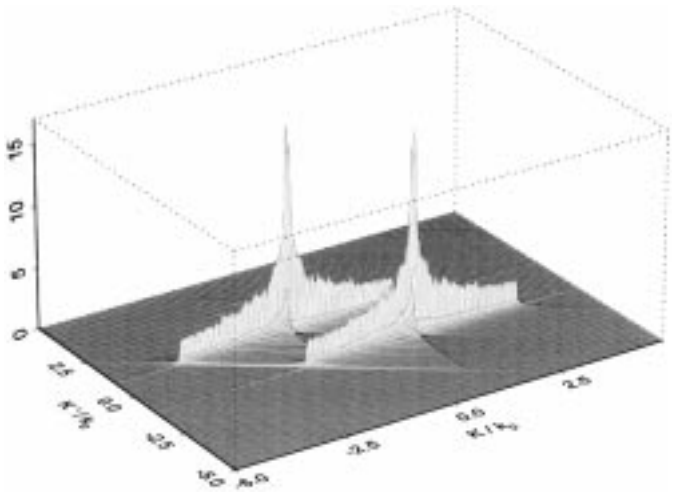

Fig. 12. Two-dimensional Fourier spectrum of the propagator (linear scale single realization of a P–M surface). Horizontal polarization, surface spectral cutoff is $2.5k_0$.

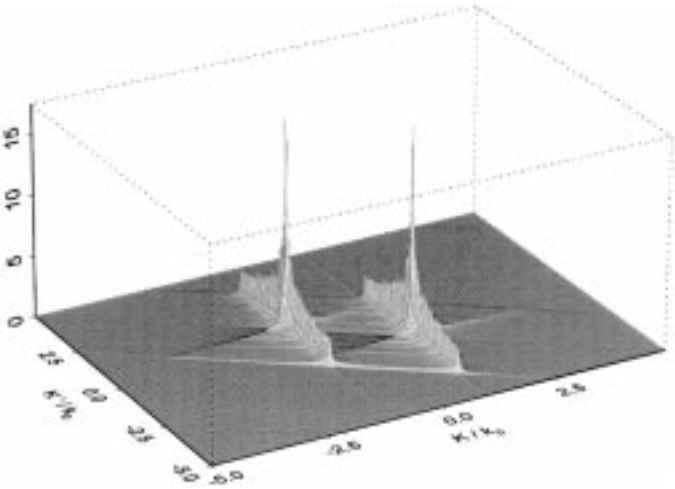

Fig. 13. Two-dimensional Fourier spectrum of the propagator (linear scale single realization of a P–M surface). Vertical polarization, surface spectral cutoff is $2.5k_0$.

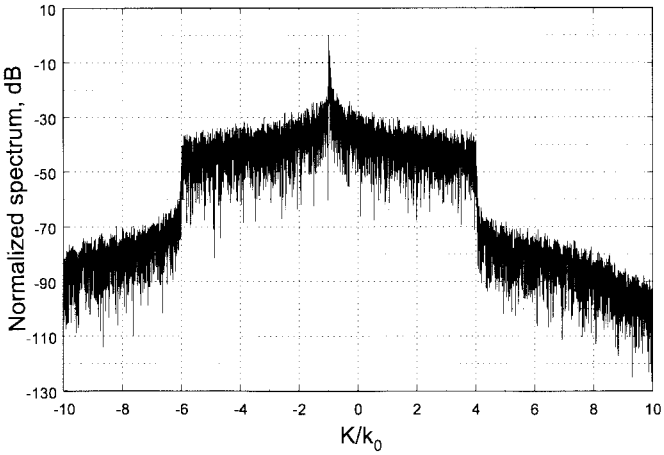

Fig. 14. Example of the Fourier spectrum of the Kirchhoff current (single realization of a P–M surface). Horizontal polarization, $\theta_i = 80°$, surface spectral cutoff is $5k_0$.

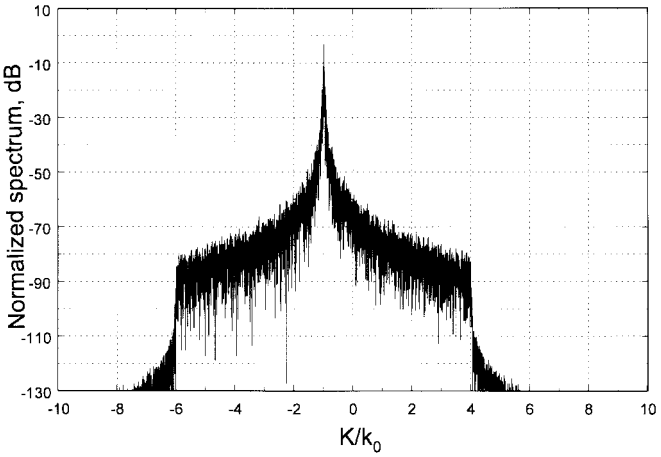

Fig. 15. Example of the Fourier spectrum of the Kirchhoff current (single realization of a P–M surface). Vertical polarization, $\theta_i = 80°$, surface spectral cutoff is $5k_0$.

logarithmic scale in Figs. 14 and 15 for horizontal and vertical polarizations, respectively, and $\theta_i = 80°$. In these examples a surface realization with the "usual" spectral cutoff of $5k_0$ [as in (21)] was used. The level of the pedestal can be different depending on the incident angle and polarization. In the case of horizontal polarization, it is higher because a derivative is involved in $J^i(x)$ in (3a) and as one moves toward grazing, this pedestal can contain an appreciable fraction of the spectral energy. The pedestal extends within the wavenumber range between $-k_0 \sin \theta_i \pm K_e$. So if we want to treat $J^i(x)$ as a band-limited function, (39) is also a reasonable choice for all incident angles.

Spectra of the currents $J(x)$ for horizontal and vertical polarizations are shown in Figs. 16 and 17, again, for $\theta_i = 80°$. These currents also exhibit the pedestal mentioned above and can be considered band-limited functions with K_u given by (39). In fact, the MFIE in (1) can be rewritten in the spectral domain as (symbols with tilda sign denote spectra of the corresponding quantities)

$$\tilde{J}(K) = \tilde{J}^i(K) + \frac{1}{2\pi} \int_{-\infty}^{\infty} \tilde{P}(K, -K') \tilde{J}(K')\, dK' \quad (40)$$

which suggests that if $P(x, x')$ and $J^i(x)$ are band-limited, $J(x)$ must also be a band-limited function since the right-hand side in (40) is then zero for $K > K_u$.

Let us point out once again that at moderate incident angles away from grazing the pedestal described above is still observed in the spectra of both $J^i(x)$ and $J(x)$, although this pedestal may now contain a lesser fraction of spectral energy compared to the main spectral peak at $-k_0 \sin \theta_i$. In any case, these spectra may be regarded as band-limited with the choice of the upper spectral limit K_u from (39) being adequate or even more than adequate for all incident angles.

Once $P(x, x')$, $J^i(x)$, and $J(x)$ are treated as band-limited functions, a moment method approach described at the beginning of this section can be applied with $\{s_n(x)\}$ from (36) serving as both the expansion and testing functions. K_u is taken from (39) and this, in turn, determines an appropriate

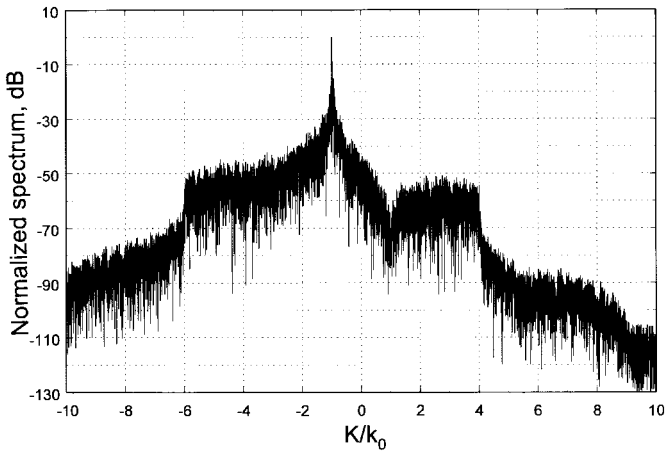

Fig. 16. Example of the Fourier spectrum of the surface current (single realization of a P–M surface). Horizontal polarization, $\theta_i = 80°$, two MOMI iterations, surface spectral cutoff is $5k_0$.

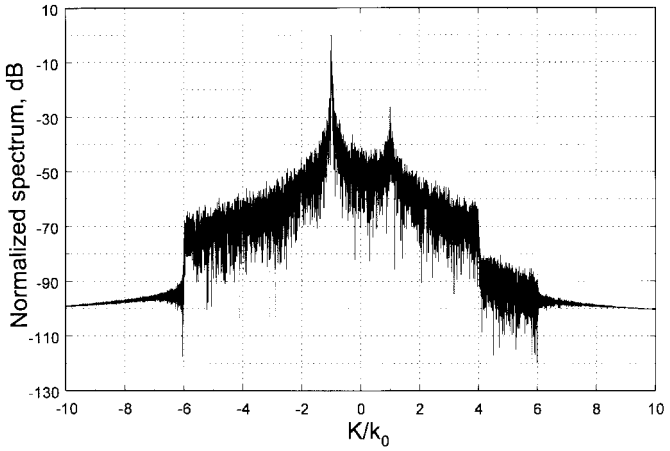

Fig. 17. Example of the Fourier spectrum of the surface current (single realization of a P–M surface). Vertical polarization, $\theta_i = 80°$, two MOMI iterations, surface spectral cutoff is $5k_0$.

sampling interval Δx in (36) as

$$\Delta x = \frac{\pi}{k_0 + K_c} = \frac{\lambda_0}{2(1 + K_c/k_0)}. \tag{41}$$

Elements of vectors and matrix in (34) can be rewritten using (38) [with $a_m = \Delta x$, as can be seen comparing (33) to (37)]. The expression for P_{mn} in (34) involves a 2-D scalar product defined similarly to (30) and it then can be related to the samples of $P(x, x')$ through a 2-D version of (38), namely $\langle s_m(x)s_n(x'), f(x, x')\rangle/(\Delta x)^2 = f(m\Delta x, n\Delta x)$. Thus, we finally do arrive at the discretization shown in (10).

Note that this approach clearly requires that the values for the diagonal terms for the propagator should be just the samples of the propagator taken at the same point $x = x' = m\Delta x$: $P_{mm} = P(m\Delta x, m\Delta x)\Delta x$. As was mentioned, though the value of $P(x, x')$ from (2b), (4) or (3b), (5) at such points is indeterminate (behaving as 0/0), it can be shown that the limit does exist and is given by

$$\lim_{x' \to x} P(x, x') = \pm \frac{\zeta_{xx}(x)}{2\pi[1 + \zeta_x^2(x)]} \tag{42}$$

(the upper sign corresponds to the vertical polarization and the lower to the horizontal). Upon multiplying (42) by Δx and substituting $x = m\Delta x \equiv x_m$ we get for the diagonal elements of the propagator matrix exactly the "curvature term" given in (15). So, the important conclusion of the sampling approach outlined above is that the curvature term should appear on the diagonal of the propagator matrix and it is not an additional correction. When we leave the curvature terms out, we, in fact, solve the MFIE with an altered kernel and this is bound to produce the kind of differing results we saw in the Section III no matter what particular numerical technique is applied to solve the MFIE. Indeed, we saw (cf. Figs. 2 and 3) that if the curvature term is not included, MOMI still converges rapidly, but it converges to different answers. It simply means that at each given sampling interval MOMI finds the solution to the MFIE with a perturbed propagator. Another important conclusion is that the off-diagonal terms should be just samples of the propagator as well as the diagonal elements should only contain the curvature terms (15). Once the proper sampling interval such as given in (41) is chosen, there is no reason to include any additional correction terms like ones that may arise from the evaluation of (35) by expansion of the integrand in a Taylor series or to expect that these higher order terms will improve the accuracy of the solution.

It should be pointed out that the inclusion of the surface curvature in the numerical algorithm by no means complicates it since the values for surface curvature can be easily generated together with surface heights and slopes using the spectral technique outlined in Section III.

Let us finally address a question of calculating the scattered field. The far-field propagator Q [given by (7) and (8)] also can be treated as band-limited functions with a spectrum concentrated within the limits of $\pm K_u$ as given in (39). Upon substitution of the expansion (31) for $J(x)$ and applying (38), the integral in (6) can be written as a discrete sum

$$\int_{\mathrm{X}} Q(x, \theta_s)J(x)\,dx = \sum_n J_n \int_{\mathrm{X}} s_n(x)Q(x, \theta_s)\,dx = \Delta x \sum_n J_n Q(n\Delta x, \theta_s). \tag{43}$$

So, the scattered field can be calculated from the sampled surface current and the similarly sampled propagator Q.

We can compare the sampling interval suggested in (41) to what we were using in Section III. Our largest sampling interval there was, from (27), $\Delta x_0 = \lambda_0/10$, while for the chosen spectral cutoff in (21) formula (41) gives a smaller value of $\Delta x = \lambda_0/12$. Indeed, in Fig. 7 we noticed a slight change in the phase of the calculated field (with included curvature term) as the sampling interval changed from Δx_0 to $\Delta x_0/2$ (which is less than $\lambda_0/12$). Still the change is very small, which suggests that quite accurate results may be possible with somewhat larger sampling intervals than given by (41). From Fig. 9, we saw that relative mean square error in the current at $\Delta x_0 = \lambda_0/10$ for the surface with a cutoff given by (21) is still below -60 dB. However, we believe that the sampling interval should not be larger than π/K_c since otherwise the surface structure will not be represented correctly (due to spectral aliasing effects). Also, we would

like to point out that (41) should not be applied to surfaces with low spectral cutoffs (say, below $2k_0$), especially if the backscattered field at LGA's is of interest. This is because for such low cutoffs it will be mainly the spectral components of the current outside the pedestal, which is now quite "narrow" due to the small cutoff, that are responsible for the low-grazing scattered field [one can see it by writing the integral in (6) in terms of Fourier spectra of J and Q] and these components will be sensitive to the spectral aliasing due to their extremely small amplitude. In fact, some differences in NRCS that we saw in Fig. 4 are probably due to these effects. In a sense, these "low-cutoff" surfaces might prove to be "tougher" for low-grazing backscattering calculations and require even tighter sampling than P–M surfaces with high cutoffs like (21).

V. Conclusion

Numerical simulations of scattering from the Pierson–Moskowitz surfaces show that if the curvature term is not included in the diagonal of the propagator in the discretized MFIE, the results can exhibit excessive sensitivity to the sampling interval and may require very tight sampling to reach the stable value. This effect is especially significant for the scattering at LGA's in the case of horizontal polarization and has an impact on average quantities such as the average normalized radar cross section. However, when the curvature terms are included in the diagonal of the propagator matrix, the calculated scattered field reaches the stable value at much larger sampling interval. Careful consideration of the discretization of MFIE shows that curvature terms indeed must be included in the diagonal of the propagator, being simply the sampled values of the propagator as well as the off-diagonal elements; there should be no additional correction terms once a proper sampling interval is chosen. The recommendation for choosing such an interval when calculating scattering from Pierson–Moskowitz surfaces is given. We would also like to point out that our simulation results once again demonstrated the robustness of MOMI when applied to randomly rough surfaces—this time for the surfaces with Pierson–Moskowitz spectrum.

Acknowledgment

The authors would like to thank Dr. D. Kapp whose work laid a foundation for this research and whose comments and suggestions were always very helpful. They would also like to thank the other members of their laboratory for their interest in this work and their friendly support.

References

[1] D. A. Kapp and G. S. Brown, "A new numerical method for rough surface scattering calculations," *IEEE Trans. Antennas Propagat.*, vol. 44, pp. 711–721, May 1996.
[2] D. Holliday, L. L. DeRaad, and G. J. St-Cyr, "Forward–backward: A new method for computing low-grazing angle scattering," *IEEE Trans. Antennas Propagat.*, vol. 44, pp. 722–729, May 1996.
[3] D. A. Kapp, "A new method to calculate wave scattering from rough surfaces at low grazing angles," Ph.D. dissertation, Virginia Polytechnic Inst. State Univ., 1995.
[4] G. S. Brown and D. A. Kapp, "The effect of surface curvature on the sampling interval and convergence rate of the method of ordered multiple interactions," presented at *APS/URSI Symp.*, Baltimore, MD, July 1996; abstract *URSI Dig. USNC/URSI Radio Sci. Meet.*, Baltimore, MD, 1996, p. 144.
[5] N. Morita, N. Kumagi, and J. Mautz, *Integral Equation Methods for Electromagnetics.* Boston, MA: Artech, 1990, pp. 131–134.
[6] E. Thorsos, "The validity of the Kirchhoff approximation for rough surface scattering using a Gaussian roughness spectrum," *J. Acoust. Soc. Amer.*, vol. 83, no. 1, pp. 78–92, Jan. 1988.
[7] E. Thorsos, "Acoustic scattering from 'Pierson-Moskowitz' sea surface," *J. Acoust. Soc. Amer.*, vol. 88, no. 1, pp. 335–349, July 1990.
[8] R. Harrington, *Field Computation by Moment Methods.* New York: IEEE Press, 1993.
[9] D. Middleton, *An Introduction to Statistical Communication Theory*. New York: McGraw-Hill, 1960, pp. 210–212.

Jakov V. Toporkov (S'95) was born in Sverdlovsk (Yekaterinburg), Russia, in 1966. He received the M.S. degree (with distinction) in electronics engineering from Moscow Institute of Physics and Technology, Russia, in 1989, and the M.S. degree in physics from Virginia Tech, Blacksburg, VA, in 1996. He is currently working toward the Ph.D. degree in physics at Virginia Tech.

From 1989 to 1993, he was employed in Russia as an Engineer-Researcher involved in the design of synthetic aperture radars (SAR's). In particular, his research interests at a time included SAR imaging of moving targets. His current research interests include electromagnetic scattering by randomly rough surfaces at low grazing angles and SAR imaging of rough surfaces.

Roger T. Marchand, photograph and biography not available at the time of publication.

Gary S. Brown, (S'61–M'67–SM'81–F'86) for photograph and biography, see p. 2 of this issue.